

Three-dimensional roll-up of a viscoelastic mixing layer

By ZHAOSHENG YU¹ AND NHAN PHAN-THIEN²

¹School of Aerospace, Mechanical and Mechatronic Engineering, The University of Sydney, NSW 2006, Australia

²Division of Bioengineering, The National University of Singapore, Singapore 117576

(Received 4 March 2002 and in revised form 12 June 2003)

In this paper, the three-dimensional roll-up of a viscoelastic mixing layer is numerically simulated with the pseudospectral method using the FENE-P model. An artificial diffusion is self-adaptively introduced into the constitutive equation to stabilize the time integration. In the three-dimensional mixing layer and within the parameter ranges studied, the effect of the polymer additives on the formation of the coherent structures such as the ribs and the cups is found to be negligible. The polymer normal stresses develop wherever there exist extensional strains that are produced by the coherent structures and they then hinder the development of these structures. Stretching by the quadrupoles and the ribs together gives rise to an enormous enhancement of the polymer normal stress differences in the symmetrical plane between the quadrupole pair. These normal stress differences directly or indirectly weaken all large-scale structures occurring in the flow including the quadrupoles, the cups, the ribs, the spanwise vortices which rotate in the opposite direction to that of the cups, and the thin spanwise vortical sheets. Attenuation of these large-scale structures leads to a diminution of small-scale structures after their breakdown in the secondary roll-up process of the thin sheets. There is a tendency for the small-scale structures in the core region to merge into a large-scale one in the viscoelastic case. As a result, a flat and inclined vortex forms at the end of the simulation which resembles the type of structure observed in an experimental mixing layer with surfactants injected. In addition, the results show that the extensional viscosity is an important quantity to determine the extent to which the coherent structures in a mixing layer are modified by polymer additives.

1. Introduction

The mixing layer is an important model for the investigation of turbulence in free shear layers and is commonly encountered in various natural flows and in industrial equipment (e.g. combustor). Over the past thirty years, the coherent structures in Newtonian mixing layers, known as the spanwise vortices (rollers) as a result of Kelvin–Helmholtz instability and the streamwise counter-rotating vortices, have been the subject of extensive studies (e.g. Lasheras & Choi 1988; Nygaard & Glezer 1991; Rogers & Moser 1992; Leboeuf & Mehta 1996). The behaviour of the coherent structures in a mixing layer has been well understood, see Rogers & Moser (1992) for a review. Nevertheless, works aimed at elucidating the effects of polymer additives on a mixing layer are limited. Experimental results reported by Hibberd, Kwade & Scharf (1982) and Riediger (1989) showed a longer lifetime of large-scale coherent structures

and a diminution of small-scale structures in the presence of polymer additives. The linear stability analyses (Azaiez & Homsy 1994a; Azaiez 2000) indicated that both polymer and fibre additives could inhibit the instability in two-dimensional mixing layers. The numerical simulation of two-dimensional nonlinear instabilities were conducted by Azaiez & Homsy (1994b) and Kumar & Homsy (1999) using the FENE-P model, and Yu, Lin & Fan (1999) using a multi-bead rigid-rod-like polymer model. Azaiez & Homsy (1994b) observed the build-up of high polymer normal stresses along the extensional axes surrounding the spanwise vortex, vorticity intensification in the braid region, and a slightly longer lifetime and a higher intensity of the vortex in the viscoelastic case. Yu *et al.* (1999) compared a Newtonian mixing layer and a viscoelastic one at the same Reynolds number based on solvent viscosity. The results revealed that the addition of polymers always led to a weakened roll-up process and a vortex of a lower intensity. In these two studies, the effect of elasticity on flow fields was so small that a significant departure of the streamline structure from the Newtonian case was not detected. Kumar & Homsy (1999), on the other hand, examined the flow field that was substantially modified by the polymer elasticity. At a ratio of Weissenberg to Reynolds number E of order unity, and a sufficiently large polymer extensibility parameter b in the FENE-P model, they found that the fundamental perturbation was not dominant and the roll-up process was inhibited. In addition, they calculated the growth rates of three-dimensional perturbations which were introduced to the two-dimensional quasi-steady states, showing that the flow became more stable at large enough values of E and b . They suggested a mechanism for the polymer-induced drag reduction that polymer additives prevented the formation of regions of concentrated vorticity whose breakdown would give rise to small-scale turbulence. Recently, Cadot & Kumar (2000) observed in their experiments that polymer additives inhibited the formation of coherent structures in a wake flow.

It is well known that an addition of a small amount of polymer to a wall-bounded turbulent flow can result in a substantial drag reduction (Lumley 1969). There is abundant experimental (e.g. Oldaker & Tiederman 1977) and numerical (e.g. Sureshkumar, Beris & Handler 1997; Yarin 1997; Dimitropoulos, Sureshkumar & Beris 1998) evidence showing that the drag-reduction mechanism is related to the negative effect of polymer additives on the formation of streamwise vortices in the near-wall flows. The streamwise vortices enhanced the small-scale motion in a mixing layer significantly and played an important role in the transition to turbulence (Nygaard & Glezer 1991). However, it remains unknown how polymer additives modify the behaviour of the streamwise vortices in a mixing layer. In this study, the roll-up of a three-dimensional viscoelastic mixing layer is numerically simulated and the roles of polymer additives in the formation and evolution of the coherent structures are elucidated in an attempt to answer the following questions:

- (i) Are the formation and the development of the three-dimensional coherent structures including the streamwise vortices really suppressed by polymer additives?
- (ii) If so, in what way do polymer additives affect the coherent structures?

In order to better understand the dynamic behaviour of the coherent structures in a mixing layer, the initial disturbances are only composed of two types of low-wavenumber ones which are specially designed to generate the rollers and the counter-rotating streamwise vortices, respectively. As a result, the flow is more similar to the forced experimental mixing layer in which the inlet disturbances are controlled much in the same manner as in Lasheras & Choi (1988). In this study, only the roll-up instability and the subsequent transition process are of interest, and the effects of

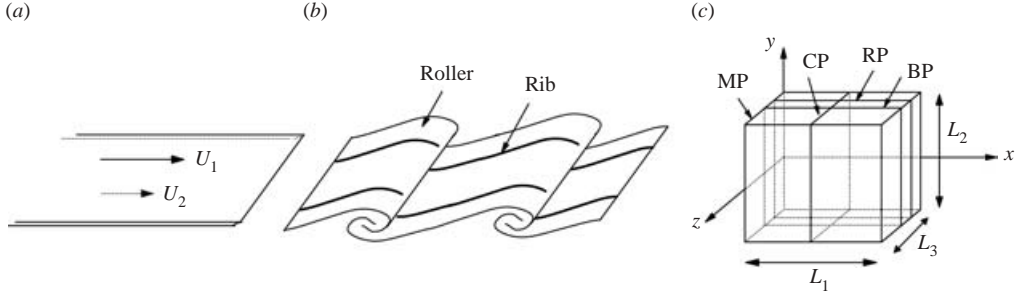


FIGURE 1. Diagram of a plane mixing layer. The computational domain is a periodic box (c).

polymer additives on the pairing instability and the fully developed turbulent flow will not be addressed. Nygaard & Glezer (1991) found that the transition in a forced mixing layer subjected to spanwise-non-uniform excitations is possible in the absence of pairing.

In §2, we describe the governing equations, our numerical method, and the definitions of some quantities used in this study for analysing the results. In §3, we examine the effects of polymers on a two-dimensional mixing layer, and then the three-dimensional results are presented and discussed. The conclusions are given in the last section.

2. Numerical model

2.1. Governing equations

Figure 1 shows the standard mixing layer arising from the two parallel streams with difference velocities U_1 and U_2 , respectively. We denote by $u_0 = (U_1 - U_2)/2$ the free-stream velocity in a reference frame moving with the average velocity of the flow $(U_1 + U_2)/2$, and by θ_0 the initial momentum thickness of the mixing layer. The main stream velocity difference $U = 2u_0$ is taken as the characteristic velocity and $\delta_0 = 2\theta_0$ as the characteristic length. Thus, the Reynolds number is defined by $Re = \rho U \delta_0 / \eta_0$, and the Weissenberg number, $We = U \lambda / \delta_0$; here, ρ , η_0 and λ are the density, the zero-shear-rate viscosity and the relaxation time of the fluid, respectively.

The dimensionless governing equations include the continuity, the momentum, and the FENE-P constitutive equations:

$$\nabla \cdot \mathbf{v} = 0, \quad (2.1)$$

$$\frac{\partial \mathbf{v}}{\partial t} + \nabla(p + \frac{1}{2} |\mathbf{v}|^2) = \mathbf{v} \times \boldsymbol{\omega} + \frac{k}{Re} \nabla^2 \mathbf{v} + \frac{1}{Re} \nabla \cdot \boldsymbol{\tau}, \quad (2.2)$$

$$f \mathbf{B} + We \left(\frac{\partial \mathbf{B}}{\partial t} + \mathbf{v} \cdot \nabla \mathbf{B} - \nabla \mathbf{v}^T \cdot \mathbf{B} - \mathbf{B} \cdot \nabla \mathbf{v} \right) = \mathbf{I}, \quad (2.3)$$

$$\boldsymbol{\tau} = \frac{(1-k)}{We} (f \mathbf{B} - \mathbf{I}), \quad (2.4)$$

$$f = \frac{1-3/b}{1-\text{tr}(\mathbf{B})/b}, \quad (2.5)$$

where \mathbf{v} denotes velocity, p pressure, $\boldsymbol{\omega}$ vorticity, k the ratio of the solvent viscosity η_s to the zero-shear-rate viscosity η_0 , \mathbf{B} the polymer conformation (structure) tensor, \mathbf{I} the unit tensor, $\boldsymbol{\tau}$ the polymer stress tensor and b , a parameter representing the maximum extensibility of polymers. $\boldsymbol{\tau}$ has been scaled to $\eta_0 U / \delta_0$ and p to ρU^2 . The FENE-P

model has been used to successfully simulate two-dimensional mixing-layer flows (Azaiez & Homsy 1994*b*; Kumar & Homsy 1999) and the turbulent channel flows (Dimitropoulos *et al.* 1998); later on, we also consider the PTT model (Phan-Thien & Tanner 1977) very briefly.

The time-developing mixing layer is considered here, for which periodic boundary conditions are imposed in both streamwise and spanwise directions. To simplify the computation, we impose the free-slip boundary condition in the transverse direction at a finite distance (but far) away from the centre of the flow field. In other words, what we are interested in is a flow between two smooth walls, which, however, is a good approximation to a mixing layer of an infinite domain before the eddies reach the walls. In fact, real mixing-layer flow also occurs in a finite domain. We set $L_2 = 12$ for the two-dimensional case and $L_2 = 24$ for the three-dimensional case, which will be verified as appropriate values later.

The initial velocity field for the time-developing plane mixing layer consists of the following three parts:

(a) a base flow with hyperbolic-tangent profile

$$u_0 = 0.5 \tanh(y); \quad (2.6)$$

(b) a two-dimensional fundamental disturbance, the streamfunction of which is

$$\Psi(x, y) = A_1 Re\{\phi_1(y) \exp(i\alpha_1 x)\}, \quad (2.7)$$

where A_1 is the amplitude, α_1 represents the wavenumber and ϕ_1 denotes the normalized eigenfunction. α_1 in this study is set at 0.4446, corresponding to the most unstable perturbation from the inviscid linear stability theory (Michalke 1964). We fix $A_1 = 0.1$ throughout this paper;

(c) and a streamwise-invariant three-dimensional perturbation with the following vorticity distribution

$$\omega_x(y, z) = A_3 \exp(-y^2/2) \sin(\beta z), \quad (2.8)$$

where β represents the spanwise wavenumber, and is taken to be one and a half the value of the streamwise wavenumber α_1 in this study, since it was found that the three-dimensional disturbance with this β is the least stable (Lasheras & Choi 1988). A_3 is fixed at 0.1. Eigenfunction is not used for the above streamwise-invariant three-dimensional perturbations because there are no eigenfunctions that satisfy the boundary conditions, as pointed out by Rogers & Moser (1992, hereinafter referred to as RM).

The above initial conditions are similar to those adopted by RM, which can produce structures of the type commonly observed in experimental mixing layers. The initial mean polymer stress field can be determined from the constitutive equations (2.3–2.5) with the base flow given in equation (2.6), reported in the Appendix. It is not possible to obtain the initial disturbance polymer stresses from the linear stability theory since the three-dimensional velocity disturbances even in the Newtonian case cannot be determined from the linear stability theory. Therefore, we evaluate the initial disturbance polymer stresses from the linearized constitutive equations with initial velocity fields given above. In this study, we are only concerned with the effects of a small amount of the long-chain polymer additives on the high-Reynolds-number flows, i.e. high Re , high k , high b and low We/Re . For this case, the two-dimensional linear stability analysis (Azaiez & Homsy 1994*a*) indicated that viscoelasticity has negligible effects on the stability behaviour of the flow, and we found that simply discarding the initial disturbance stress results in only negligible differences in the

evolution of the flows. However, in the case of small k , it is necessary to incorporate the disturbances into the initial stress conditions, otherwise, the reduction in the diffusion of velocity disturbances at early time due to the non-unity k (see equation (2.2)) would contaminate (or seemingly enhance) the pure effect of the shear thinning to some extent.

The passive scalar represents a quantity that can be convected and diffused in the flow such as temperature and mass concentration and consequently is often used to conduct a numerical dye visualization. The passive scalar is computed by using the following equation

$$\frac{\partial T}{\partial t} + \mathbf{v} \cdot \nabla T = \frac{1}{Pe} \nabla^2 T, \quad (2.9)$$

where Pe denotes the Péclet number and is set to be 400. The initial condition is given by

$$T = 0.5[1 + \tanh(y)]. \quad (2.10)$$

2.2. Numerical method

The computational domain is shown in figure 1, with both periods in the streamwise direction L_1 and in the spanwise direction L_3 equal one wavelength of the fundamental modes in their own directions, respectively. The standard fast Fourier transform (FFT) is applied in all three directions and the governing equations in the spectral space with the pressure eliminated (with the mass conservation constraint $\boldsymbol{\alpha} \cdot \mathbf{v}^* = 0$, where $\boldsymbol{\alpha} = (2\pi m/L_1, 2\pi n/2L_2, 2\pi l/L_3)$ denoting the wavenumber vector of the Fourier modes) are written as

$$\frac{\partial \mathbf{v}^*}{\partial t} + \frac{k |\boldsymbol{\alpha}|^2}{Re} \mathbf{v}^* = \mathbf{f}^* + \mathbf{g}^* - \frac{\boldsymbol{\alpha}(\boldsymbol{\alpha} \cdot (\mathbf{f}^* + \mathbf{g}^*))}{|\boldsymbol{\alpha}|^2}, \quad (2.11)$$

$$\frac{\partial \mathbf{B}^*}{\partial t} = \mathbf{Q}^*, \quad (2.12)$$

in which \mathbf{f} , \mathbf{g} and \mathbf{Q} are defined by

$$\mathbf{f} = \mathbf{v} \times \boldsymbol{\omega}, \quad (2.13)$$

$$\mathbf{g} = \frac{1}{Re} \nabla \cdot \boldsymbol{\tau}, \quad (2.14)$$

$$\mathbf{Q} = -\mathbf{v} \cdot \nabla \mathbf{B} + \mathbf{B} \cdot \nabla \mathbf{v} + (\nabla \mathbf{v})^T \cdot \mathbf{B} + \frac{(\mathbf{I} - \mathbf{f} \mathbf{B})}{We}. \quad (2.15)$$

Equations (2.11)–(2.12) are advanced in time with a second-order Crank–Nicolson–Adams–Bashforth scheme:

$$\frac{\mathbf{B}^{*n+1} - \mathbf{B}^{*n}}{\Delta t} = \frac{1}{2}(3\mathbf{Q}^{*n} - \mathbf{Q}^{*n-1}), \quad (2.16)$$

$$\begin{aligned} \frac{\mathbf{v}^{*n+1} - \mathbf{v}^{*n}}{\Delta t} + \frac{k |\boldsymbol{\alpha}|^2}{Re} \frac{\mathbf{v}^{*n+1} + \mathbf{v}^{*n}}{2} &= \frac{1}{2}(3\mathbf{f}^{*n} - \mathbf{f}^{*n-1}) + \frac{\mathbf{g}^{*n+1} + \mathbf{g}^{*n}}{2} \\ &\quad - \frac{1}{2} \frac{\boldsymbol{\alpha} \{ \boldsymbol{\alpha} \cdot [(3\mathbf{f}^{*n} - \mathbf{f}^{*n-1}) + (\mathbf{g}^{*n+1} + \mathbf{g}^{*n})] \}}{|\boldsymbol{\alpha}|^2}. \end{aligned} \quad (2.17)$$

Nonlinear terms \mathbf{f} and \mathbf{Q} are computed in the physical space and then transformed into the spectral space, leading to the so-called pseudospectral method. The aliasing errors are removed by using the truncation method (Canuto *et al.* 1987).

The initial velocity field is symmetric about the plane $z = L_3/2$, which is preserved by the governing equations. Hence, the efficient fast sin/cos transformations can be used as a substitute for the standard FFT in both the transverse and the spanwise directions. The components of the velocity vector and the conformation tensor are divided into four groups according to their base functions in two directions:

$$\left. \begin{aligned} & \left\{ \cos\left(\frac{\pi ny}{L_2}\right) \cos\left(\frac{\pi lz}{L_3/2}\right) \right\} : u, B_{xx}, B_{yy}, B_{zz}, \\ & \left\{ \cos\left(\frac{\pi ny}{L_2}\right) \sin\left(\frac{\pi lz}{L_3/2}\right) \right\} : w, B_{xz}, \\ & \left\{ \sin\left(\frac{\pi ny}{L_2}\right) \cos\left(\frac{\pi lz}{L_3/2}\right) \right\} : v, B_{xy}, \\ & \left\{ \sin\left(\frac{\pi ny}{L_2}\right) \sin\left(\frac{\pi lz}{L_3/2}\right) \right\} : B_{yz}. \end{aligned} \right\} \quad (2.18)$$

The equations in the new spectral space are essentially the same as those given above, and slight modifications are required only for the terms involving a first-order spatial differential. The subroutines for the one-dimensional fast Fourier, and cosine and sine transforms are available in Press *et al.* (1996).

2.3. Introduction of artificial diffusion

It was found that the accumulation of numerical error during time integration can lead to a loss of positive definiteness for the conformation tensor and then a numerical instability (Sureshkumar & Beris 1995) sets in. For the pseudospectral method, a simple and computationally efficient remedy is to introduce an artificial diffusive term into the constitutive equation. In our case, equation (2.16) is simply replaced with

$$\frac{\mathbf{B}^{*n+1} - \mathbf{B}^{*n}}{\Delta t} + \nu_a |\boldsymbol{\alpha}|^2 \mathbf{B}^{*n+1} = \frac{1}{2}(3\mathbf{Q}^{*n} - \mathbf{Q}^{*n-1}), \quad (2.19)$$

in which ν_a is the stress diffusivity. We introduce a stress diffusivity coefficient a so that $\nu_a = ah_2^2$, here h_2 is the transverse mesh size, considering the fact that ν_a should be decreased with mesh refinement. In previous works, ν_a is kept invariable during the entire simulation. A small enough value of ν_a was found to be capable of enhancing the stability considerably without altering the flow dynamics for sufficiently fine spatial discretization (Sureshkumar & Beris 1995). Equation (2.19) can be re-written as follows

$$\mathbf{B}^{*n+1} = \frac{\mathbf{B}^{*n} + \frac{1}{2}\Delta t(3\mathbf{Q}^{*n} - \mathbf{Q}^{*n-1})}{1 + \nu_a \Delta t |\boldsymbol{\alpha}|^2}. \quad (2.20)$$

Clearly, the artificial diffusion scheme outlined above is equivalent to a filtering of the Fourier coefficients at every time step with the filter

$$\sigma(k_1, k_2, k_3) = 1/(1 + \nu_a \Delta t |\boldsymbol{\alpha}|^2). \quad (2.21)$$

The filtering technique is widely used to deal with shock problems. Some classical filters such as the Lanczos filter and the raised cosine filter (Canuto *et al.* 1987) were also tested to solve the constitutive equation. We found that the resulting solution for each filter is influenced by the intensity of the filter ν_a (or the number of time steps between applications of the filter N_f), but all solutions are reasonably accurate if the values of ν_a or N_f are judiciously chosen.

A simple method with the adaptive artificial diffusivity is used in this study. a is set to be a_0 initially and may be modified at each time step by inspecting the trace of the conformation tensor:

$$a^{n+1} = \begin{cases} a^n \times 2 & \text{if } \text{tr}(\mathbf{B}^n) < s, \\ a^n/2 & \text{if } \text{tr}(\mathbf{B}^n) \geq s, a^n > a_0. \end{cases} \quad (2.22)$$

The value of a_0 is not important as long as it is small enough (10^{-4} in this study). It is encouraging to find that this approach ensures a good solution stability in the time integration process and without introducing much artificial diffusion. Moreover, the solution is relatively insensitive to the choice of s ($0 \leq s \leq 3$). Thus, there is no need to determine a reasonable parameter value for our approach. We choose $s = 1$ throughout this study. Some numerical results to the benefit of artificial viscosity are given (figure 3); a mesh convergence test will be presented later, in § 3.2.3.

2.4. Definition of some physical quantities

Some physical quantities that characterize the development of the mixing layer are defined below.

Energy in the modes. Owing to the symmetry of the flow, the energies in the modes can be defined by

$$E_{ml} = \frac{c}{N_1 N_2 N_3} \sum_n |\mathbf{v}^*(m, n, l)|^2, \quad c = \begin{cases} 1 & \text{if } m = 0 \text{ and } l = 0, \\ 2 & \text{if } m = 0 \text{ or } l = 0, \\ 4 & \text{otherwise, i.e. } m > 0, l > 0, \end{cases} \quad (2.23)$$

where N_1 , N_2 and N_3 are the number of collocation points in the periodic box (or the Fourier modes). The energy in all three-dimensional modes ($l \neq 0$) is defined by

$$E_{3D} = \sum_m \sum_{l \neq 0} E_{ml}. \quad (2.24)$$

Streamwise circulation. Streamwise circulation that measures the intensity of streamwise vortices in a cross-section between $z = L_3/2$ and $z = L_3$ is defined by

$$\Gamma_x = \int_{-L_2/2}^{L_2/2} \int_{L_3/2}^{L_3} \omega_x \, dz \, dx = \int_{L_3/2}^{L_3} w \, dz \Big|_{y=-L_2/2}^{y=L_2/2} - \int_{-L_2/2}^{L_2/2} v \, dy \Big|_{z=L_3/2}^{z=L_3}. \quad (2.25)$$

Momentum thickness. Momentum thickness is defined by

$$\theta = \int_{-L_2/2}^{L_2/2} (0.5^2 - \overline{U}^2) \, dy, \quad (2.26)$$

in which \overline{U} is the mean streamwise velocity.

Velocity fluctuation intensities and Reynolds stress. The fluctuation intensity of the streamwise velocity is defined by

$$U_{rms} = \overline{u'^2}. \quad (2.27)$$

The Reynolds stress is defined by

$$\tau_R = \overline{-u'v'}. \quad (2.28)$$

In (2.26)–(2.28), the bar represents the spatial average over the streamwise and the spanwise periods. The fluctuating quantities are also calculated on a basis of the spatial (or phase) average.

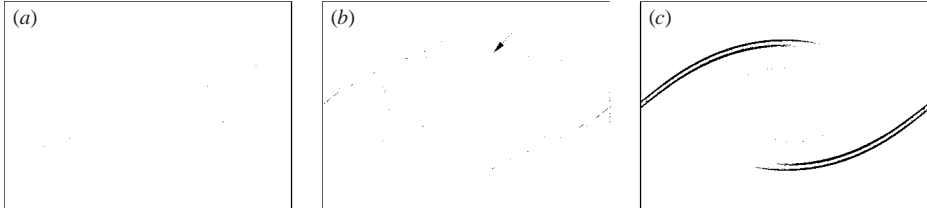


FIGURE 2. (a) $T = 40$; $(-0.46, -0.03)$; Newtonian. (b) $T = 40$; $(-0.46, -0.03)$; FENE-P. (c) $T = 40$; $(-0.05, 3.6)$. Contours of (a), (b) vorticity and (c) first normal stress difference at $Re = 200$. For (b), (c) $We = 20$, $b = 400$, $k = 0.9$, $N_1 \times N_2 = 256 \times 512$, and $\Delta t = 0.002$. The arrow in (b) points to the region of vorticity attenuation. The values in the brackets above represent the minimum and maximum contour levels, respectively. Dotted contours represent negative contour values.

3. Results and discussions

3.1. Two-dimensional results

Azaiez & Homsy (1994b) and Kumar & Homsy (1999) numerically simulated the two-dimensional roll-up of a viscoelastic mixing layer and provided good insight into the effects of viscoelasticity on the flow dynamics. However, Kumar & Homsy (1999) observed that weak viscoelasticity (small b) seems to intensify the roll-up process and the mechanism remains unidentified. We believe this viscoelasticity effect is related to the shear-thinning behaviour of the FENE-P fluid (the amount of shear-thinning at a fixed shear rate increases with increasing $We = \lambda \dot{\gamma}$ ($\dot{\gamma}$ is the shear rate) and with decreasing b), totally consistent with the observation of Kumar & Homsy (1999) that the positive effect of viscoelasticity is only present at small b and more obvious as We is increased.

Kumar & Homsy's results (1999) revealed that strong viscoelasticity (large b) will inhibit the roll-up process. The first normal stress difference builds up along the extensional axes of the spanwise vortex (as shown in figure 2c), and attenuates the vorticity at the edges of the extensional strain region (marked by an arrow in figure 2b). The vorticity attenuation speeds up the vorticity diffusion in the core and on the other hand imposes a negative effect on the concentration of the vorticity into a single vortex. When viscoelasticity is very strong, the vorticity with sign opposite to that of the mean vorticity emerges and a large-scale vortex cannot form (Kumar & Homsy 1999).

We next examine the effects of the artificial diffusion on the computational stability and the flow dynamics. It is well known that the stress concentration at high We constitutes the main difficulty in the viscoelastic flow computation. For the pseudospectral method used here, it seems possible to overcome this difficulty by continually increasing spatial and temporal resolution. For example, for the case of $We = 20$, $b = 400$, $k = 0.9$, the computation is unstable at $N_1 \times N_2 = 128 \times 128$ and $\Delta t = 0.01$ (figure 3a, d), but becomes stable at $N_1 \times N_2 = 256 \times 512$ and $\Delta t = 0.002$ (figure 2). However, the computational cost required may be prohibitively high, particularly in the three-dimensional case. When using coarse meshes, we have to introduce some artificial diffusion to stabilize the time integration. Figures 2 and 3 confirm that artificial diffusion can enhance the stability considerably without appreciably altering the flow dynamics, although it unavoidably attenuates the gradients of the normal stress and may smooth out some local small-scale structures which are otherwise caused by the high stress gradients.

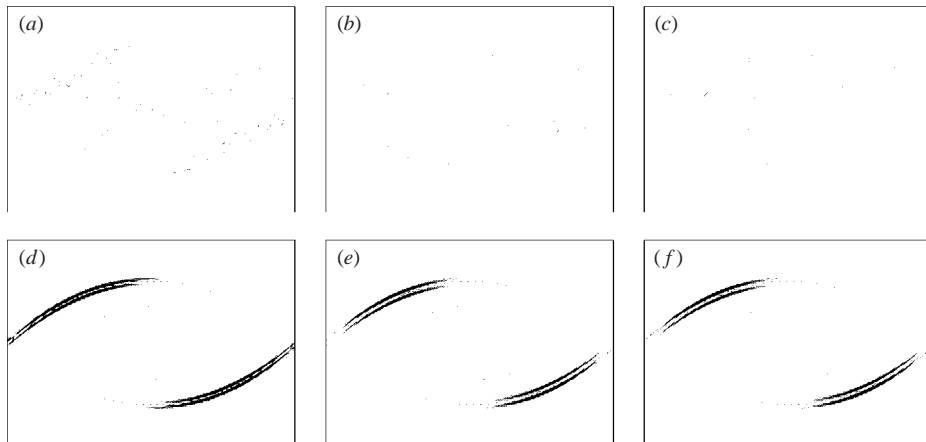


FIGURE 3. (a) $T = 40$; $(-0.46, -0.03)$. (b) $T = 40$; $(-0.46, -0.03)$. (c) $T = 40$; $(-0.46, -0.03)$. (d) $T = 40$; $(-0.05, 4.0)$. (e) $T = 40$; $(-0.05, 3.4)$. (f) $T = 40$; $(-0.05, 3.4)$. Effects of the artificial diffusion on (a), (b), (c) vorticity and (d), (e), (f) first normal stress difference. (a), (d) no artificial diffusion. (b), (e) adaptive artificial diffusivity with $s = 1$. (c), (f) constant artificial diffusivity with $a = 0.1$. $Re = 200$, $We = 20$, $b = 400$, $k = 0.9$, $N_1 \times N_2 = 128 \times 128$, $\Delta t = 0.01$. The values in parentheses represent the minimum and maximum contour levels, respectively. Dotted contours indicate negative values.

3.2. Three-dimensional results

3.2.1. Formation and evolution of coherent structures in the Newtonian case

Three-dimensional results are obtained with $N_1 \times N_2 \times N_3 = 128 \times 256 \times 64$ and $\Delta t = 0.01$. Figure 4 shows the standard structures of the streamwise rib-shaped vortices (ribs), the quadrupoles and the spanwise cup-shaped vortices (cups) in a three-dimensional plane mixing layer. Their formation processes were well-documented in RM and will be described only briefly. Following RM, we view the simulated flow mainly through four specific planes: the mid-braid plane (MP, $X = 0$), the roller core plane (CP, $X = L_1/2$), the rib plane (RP, $Z = L_3/4$), and the between-ribs plane (BP, $Z = L_3/2$), as shown in figure 1. The Kelvin–Helmholtz instability first results in the roll-up of a mixing layer. In the process, the initial weak streamwise perturbation tubes are intensified rapidly along the extensional axes owing to the stretching by the spanwise rollers, and then collapse into circular counter-rotating ribs. Meanwhile, the quadrupoles rotating in the opposite direction to that of the ribs develop at the roller core region. From figure 5(a), the quadrupole and the rib pairs together produce extensional (marked by B) and compressive (by A) strains alternately in the spanwise direction at both the top and the bottom of the regions of the rollers, resulting in the enhancement and the attenuation of the spanwise vorticity at the corresponding regions. As a result, the rollers corrugate in the spanwise direction and the cups form at the bends of the rollers. In addition to the ribs, the cups and the quadrupoles, the occurrence of the spanwise vorticity with sign opposite to that of the mean vorticity is also a manifestation of three-dimensional evolution of a mixing layer. These vortical structures first appear in the vicinity of the ribs (figure 4), and then extend in the streamwise direction under the induction of the cups. Concentrated vorticity emerges in the region adjacent to the cups (figure 5b), forming into real spanwise vortices.

Two important events are observed during the further evolution of the coherent structures before the transition to turbulence. One is the shredding of the ribs in

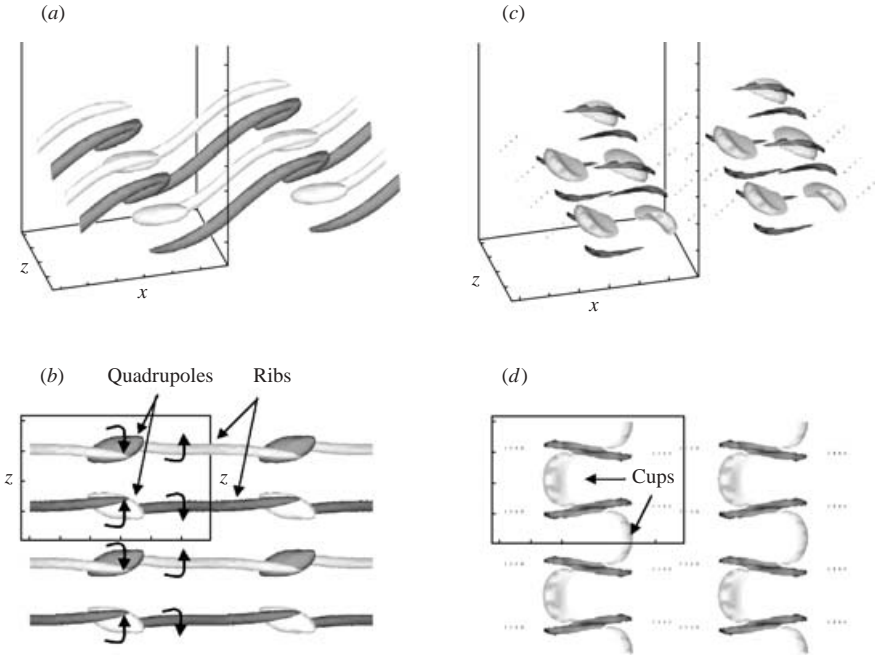


FIGURE 4. Iso-surfaces of (a), (b) streamwise vorticity showing the ribs and the quadrupoles, and (c), (d) spanwise vorticity showing the cups and occurrence of the opposite-signed vorticity in a mixing layer. (b), (d) are top views of (a), (c) respectively. The above structures inside the box are based on our numerical results for the Newtonian fluid at $Re = 200$ and $t = 40$, and those outside the box are produced with the periodicity. Dark surfaces indicate positive vorticity of 0.5 for (a), (b) and 0.1 for (c), (d), and light surfaces indicate negative vorticity of -0.5 for (a), (b) and -0.6 for (c), (d).

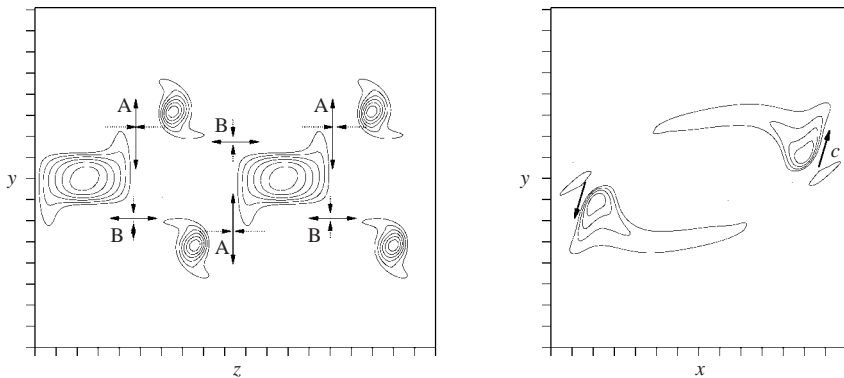


FIGURE 5. Contours of (a) ω_x in the roller core plane (CP) and (b) ω_z in the rib plane (RP). Three extensional strain fields caused by the coherent structures are shown, among which the one marked by A is most important to the viscoelastic effects. (a) $t = 40$ ($-0.6, 0.6$). (b) $t = 60$ ($-0.9, 0.4$).

the mid-braid plane and the other is the formation and the secondary roll-up of strong thin spanwise vortical sheets. It can be easily understood from figure 4 that the mutual induction between the ribs and the quadrupoles will lead both of them to tilt laterally, as shown in figure 6(a). With the quadrupoles extending towards the

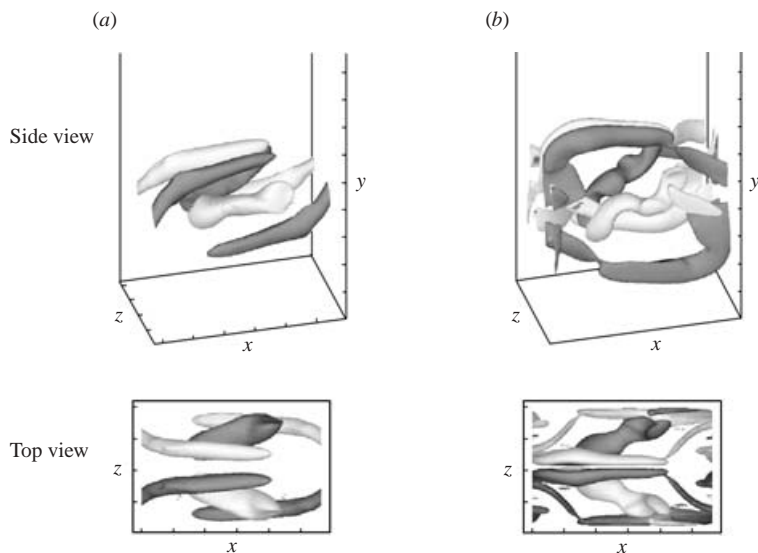


FIGURE 6. Iso-surfaces of the streamwise vorticity at (a) $t = 60$ showing lateral tilt of the ribs and the quadrupoles and (b) $t = 80$ showing shredding of the ribs at the braid region and then touch of the rib pairs in the between-rib plane for the Newtonian case at $Re = 200$. Dark surfaces indicate positive vorticity of 0.5 and light surfaces indicate negative vorticity of -0.5 for both (a) and (b).

braid region, the lateral inclination angle of the ribs and the lateral shearing force imposed on the ribs in the mid-braid plane become larger and larger, eventually resulting in the shredding of the ribs there (figure 6b). After the shredding, the rib pairs are pushed together over the whole streamwise range by the induction of the quadrupoles (figure 6b) and their interactions give rise to a substantial stretching and an enhancement of the spanwise vorticity above them (marked by D in figure 12b). As a result, strong spanwise vortical sheets form and they then undergo the secondary roll-up (figures 13a–c). Unlike the primary roll-up, a small circular vortex core with very strong vorticity occurs at about $t = 85$ as a result of a small-scale roll-up and the concentrated vorticity diffuses rapidly, which is responsible for a conspicuous vorticity pulse shown in figure 8(a). The vortical sheet finally rolls up into three vortices under the influence of the nearby opposite-signed vorticity (figure 13c). It is conceivable that the secondary roll-up of the sheets would give rise to breakdown of the ribs located just below them. Furthermore, the other vortical structures such as the quadrupoles and the spanwise vortices with sign opposite to that of the cups also break down in that process, and the flow appears ‘turbulent’ (figures 14a, 15a and 16a). RM presented similar flow characteristics after the secondary roll-up of the sheets, but they did not report events such as the shredding of the ribs and the formation and secondary roll-up of the sheets. The secondary roll-up of thin vortical sheets emerging after pairing was found to play an important role in the transition to turbulence of a mixing layer (Moser & Rogers 1991) and was observed in a stratified experimental mixing layer (Atsavaprane & Gharib 1997).

3.2.2. Effect of viscoelasticity

As mentioned earlier, we are only concerned with the effects of a small amount of the long-chain polymer additives on the high-Reynolds-number flows, i.e. high

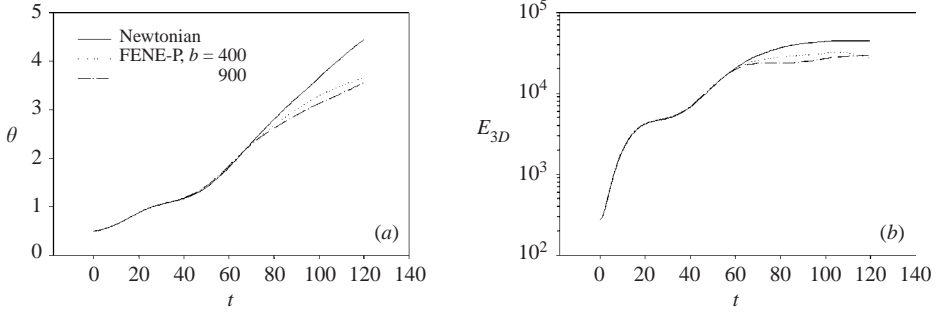


FIGURE 7. Time developments of (a) momentum thickness and (b) energies in the three-dimensional disturbances E_{3D} . $Re = 200$, $We = 20$, $k = 0.9$.

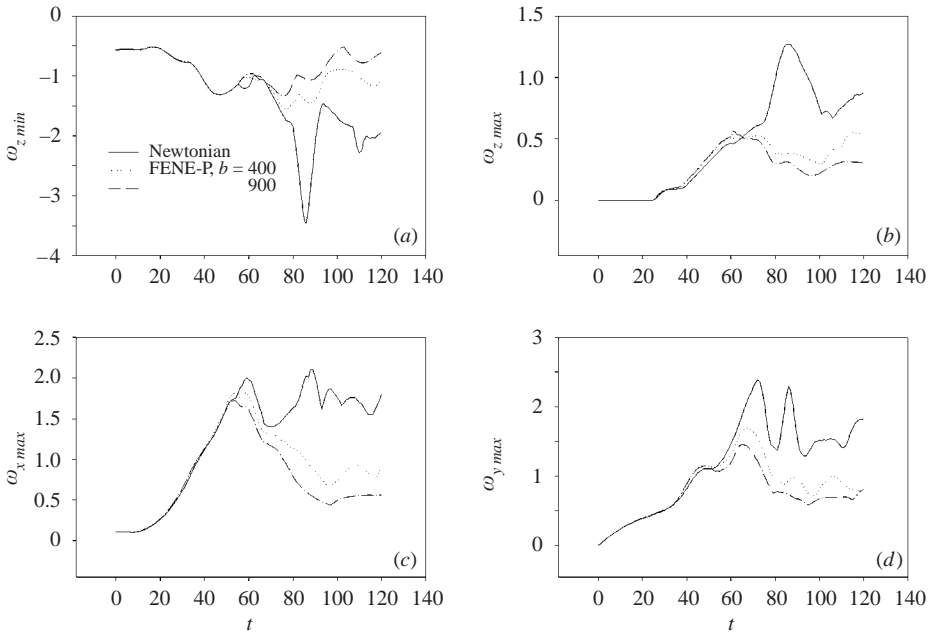


FIGURE 8. Time developments of (a) minimum of ω_z , (b) maximum of ω_z , (c) maximum of ω_x and (d) maximum of ω_y . $Re = 200$, $We = 20$, $k = 0.9$.

Re , high k , high b and low We/Re . It is well known that the polymer-induced drag reduction in the wall-bounded shear turbulence takes place under these conditions, and two experimental works on a viscoelastic mixing layer available in the literature (Hibberd *et al.* 1982; Riediger 1989) were also conducted under similar conditions. We now examine the effect of viscoelasticity on the flow mainly at two sets of parameter values. One is at $Re = 200$, $We = 20$, $k = 0.9$ and $b = 400$, and the other is at the same parameter, but with $b = 900$. For both parameter groups, the effect of the shear-thinning is expected to be very small, and we will focus on the effects of the polymer normal stresses.

Time developments of the momentum thickness, energy in the three-dimensional disturbances, the vorticity extrema and the streamwise circulations are given in figures 7–9. It can be seen from these figures that polymer additives exert negligible influence on the flow field before $t = 50$, but subsequently they dramatically reduce

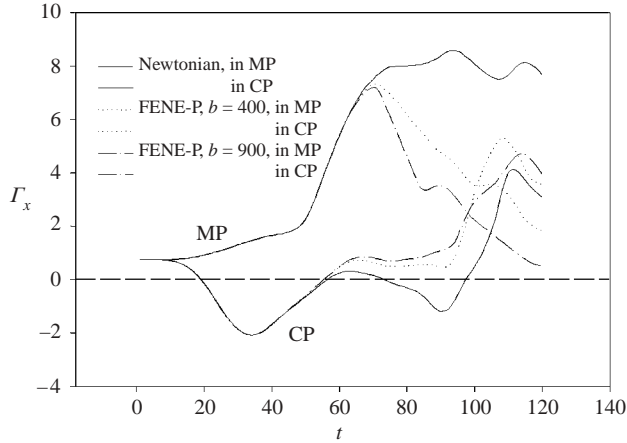


FIGURE 9. Time developments of the streamwise circulations in the mid-braid plane (MP) and the roller core plane (CP). The circulation in MP reflects the intensity of one rib there and that in CP reflects the intensity of two ribs minus the intensity of one quadrupole there during the lifetimes of the structures. $Re = 200$, $We = 20$, $k = 0.9$.

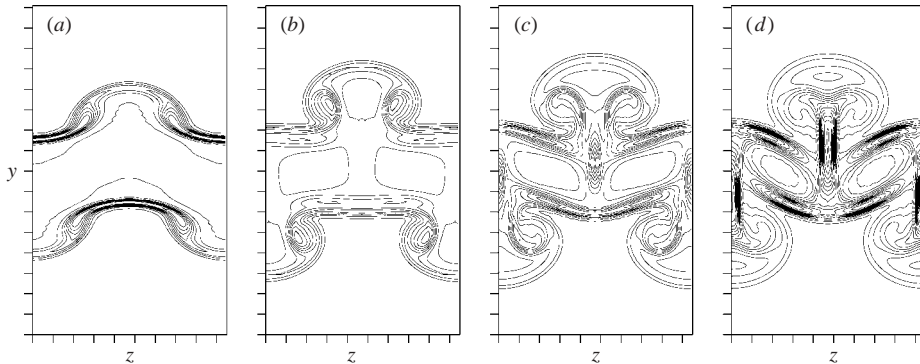


FIGURE 10. Contours of the trace of the conformation tensor $tr(\mathbf{B})$ in the roller core plane (CP). $Re = 200$, $We = 20$, $b = 400$ and $k = 0.9$. (a) $t = 30$ (20, 180). (b) $t = 40$ (20, 190). (c) $t = 50$ (20, 200). (d) $t = 60$ (20, 350).

the three-dimensionality or the inhomogeneity of the flow. Typical coherent structures including the cups, the ribs and the quadrupoles have already formed by $t = 50$, thus we can draw the conclusion that the effects of viscoelasticity on the formation of the coherent structures in a forced mixing layer are negligible.

We now investigate the behaviour of the polymer normal stresses, in order to explore the mechanism by which polymer additives affect the flow fields substantially after $t = 60$. The traces of the conformation tensor and the second normal stress differences are plotted in figure 10 and figure 11, respectively. Two-dimensional results reveal that an extensional strain field can cause substantial stretching of polymers and then a dramatic increase in the polymer normal stresses there. This mechanism still holds in the three-dimensional case. There are four conspicuous extensional strain fields in a three-dimensional mixing layer prior to $t = 60$. The first one is produced by the rollers (or the cups), as we observed in the two-dimensional case. The second and third are caused by the ribs and the quadrupoles, as shown in figure 5(a). The last

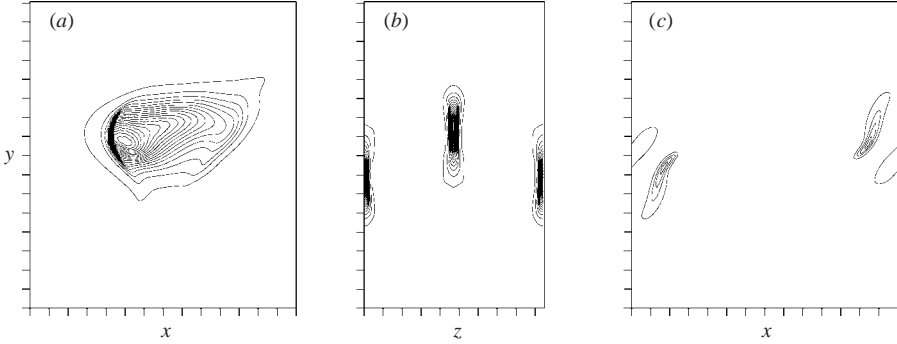


FIGURE 11. Contours of the second normal stress difference $\tau_{yy} - \tau_{zz}$ in (a) the between-rib plane (BP), (b) the roller core plane (CP) and (c) the rib plane (RP). $Re = 200$, $We = 20$, $b = 400$ and $k = 0.9$. Solid contours indicate positive stress and dotted contours indicate negative stress. (a) $t = 60$ (0.3, 23). (b) $t = 60$ (-2.0, 15). (c) $t = 60$ (-4.5, 2.1).

one is associated with the spanwise vortices that rotate in the opposite direction to that of the cups, which are expected to produce extensional strains mainly in the transverse direction (figure 5b).

The extensional strain field imposed by the rollers dominates the stretching of polymers at early time (about $t < 30$). By $t = 40$, the wrapping effect of the ribs has given rise to the appearance of a mushroom pattern for the $tr(\mathbf{B})$ in the roller core plane (figure 10b). At $t = 60$, the tilt of the ribs allows the extensional strain field in the spanwise direction caused by the quadrupoles and the ribs (marked by B in figure 5a) to extend through the rib plane, resulting in the spanwise stretching of polymers and the occurrence of negative $\tau_{yy} - \tau_{zz}$ (due to increase in τ_{zz}) in the rib plane at the core region (figures 10c, d and 11c). The extensional strain field in the transverse direction (marked by A in figure 5a) produces $tr(\mathbf{B})$ (mainly \mathbf{B}_{yy}) and accordingly τ_{yy} in BP between the ribs and quadrupoles at $t = 50$ (figure 10c). They then increase dramatically and the normal stress differences have become so large by $t = 60$ that other structures of the normal stress differences are overshadowed, as shown in figure 11(a, b). Finally, from figure 11(c), we can observe two regions of the second normal stress differences arising from the fourth strain field mentioned above.

It was made clear in the two-dimensional case that the normal stress differences building up in the extensional strain field produced by vortices play a negative role in the subsequent evolution of the vortices. All normal stress differences mentioned above behave the same way, among which the effect of the one appearing in the between-rib plane between the ribs and the quadrupoles, not surprisingly, is found to be most pronounced. It gives rise to the small regions of opposite-signed streamwise vorticity between the pair of quadrupoles and between the pair of ribs, respectively, at $t = 60$ (figure 12a, d), which weaken the induction intensities of the quadrupoles and the ribs. The attenuation of the intensities of the quadrupoles is more pronounced than that of the ribs since the contribution of one quadrupole to the streamwise circulation in the roller core plane, according to figure 9, is decreased more than that of the two ribs together. At $t = 80$, the size of the quadrupoles at the core region is appreciably reduced (figure 12b, e), and their induction intensity is accordingly diminished, which is clearly indicated by the fact that the Γ_x is positive in the viscoelastic case and negative in the Newtonian case at that time (figure 9). In addition, the effect of the normal stresses at the between-rib plane (BP) region on the cups is also significant.

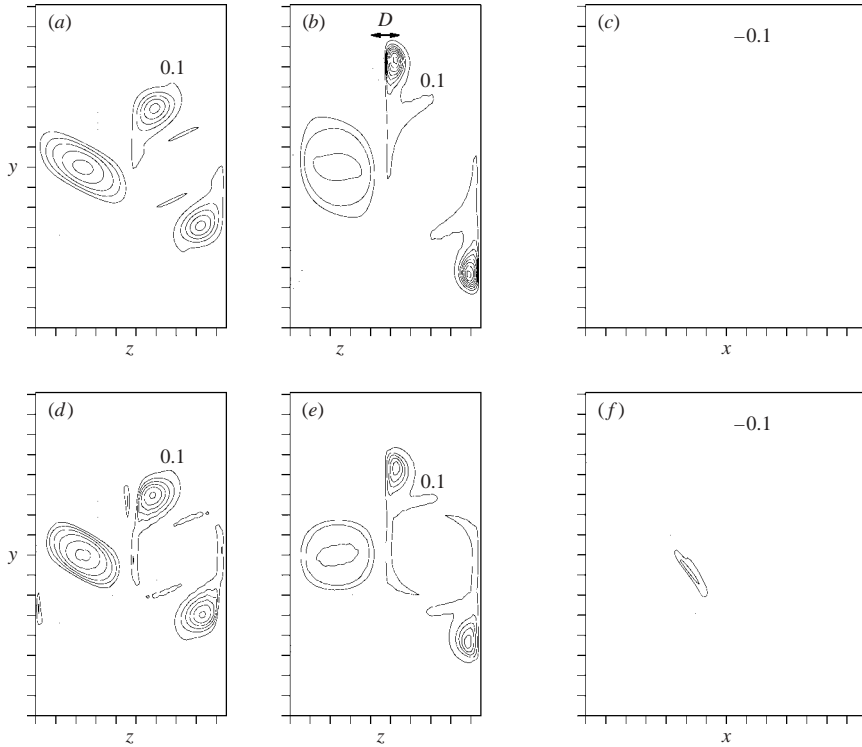


FIGURE 12. Comparisons of vorticity contours between the Newtonian case (a), (b), (c) at $Re=200$ and the viscoelastic case (d), (e), (f) at $Re=200$, $We=20$, $b=400$ and $k=0.9$. (a), (d) ω_x in the roller core plane, (b), (e) ω_x in the roller core plane and (c), (f) ω_z in the between-rib plane. Solid contours indicate positive vorticity and dotted contours indicate negative vorticity. (a) $t=60$ $(-0.9, 0.9)$. (b) $t=80$ $(-1.5, 1.5)$. (c) $t=60$ $(-0.9, -0.1)$. (d) $t=60$ $(-0.9, 0.9)$. (e) $t=80$ $(-0.9, 0.9)$. (f) $t=60$ $(-0.9, 0.2)$.

The opposite-signed vorticity caused by the large streamwise stress gradients appears near the cups (figure 12c, f) and hinders coalescence of the vorticity in the tails into the cores of the cups. As a result, two vortex cores in a viscoelastic fluid can be observed at $t=80$ and they merge into one at $t=90 \sim 110$, but the structure is not cup-shaped and much weaker in intensity than the counterpart in the Newtonian mixing layer (figure 13).

In the three-dimensional case, all sorts of vortical structures interact with each other and new types of structure may occur as a result of their nonlinear interactions. Hence, attenuation of one type of structure may lead to inhibition or retardation of the development of all other structures and the formation of new types of structures. For the three-dimensional viscoelastic mixing layer studied here, the main chain of events is as follows: viscoelasticity reduces the induction intensity of the quadrupoles, as discussed above; the resulting weaker quadrupoles lead to the weaker interaction between the ribs at the between-rib plane region (figure 12b, e); the weaker extensional strains caused by the ribs result in the weaker spanwise vortical sheets; and the weaker vortical sheets give rise to the weaker secondary roll-up of the sheets where the aforementioned vorticity pulse observed in the Newtonian case is completely inhibited (figure 8a) and only two secondary rollers result in the case of $b=400$ compared to three in the Newtonian case (figure 13). Certainly, the attenuation of

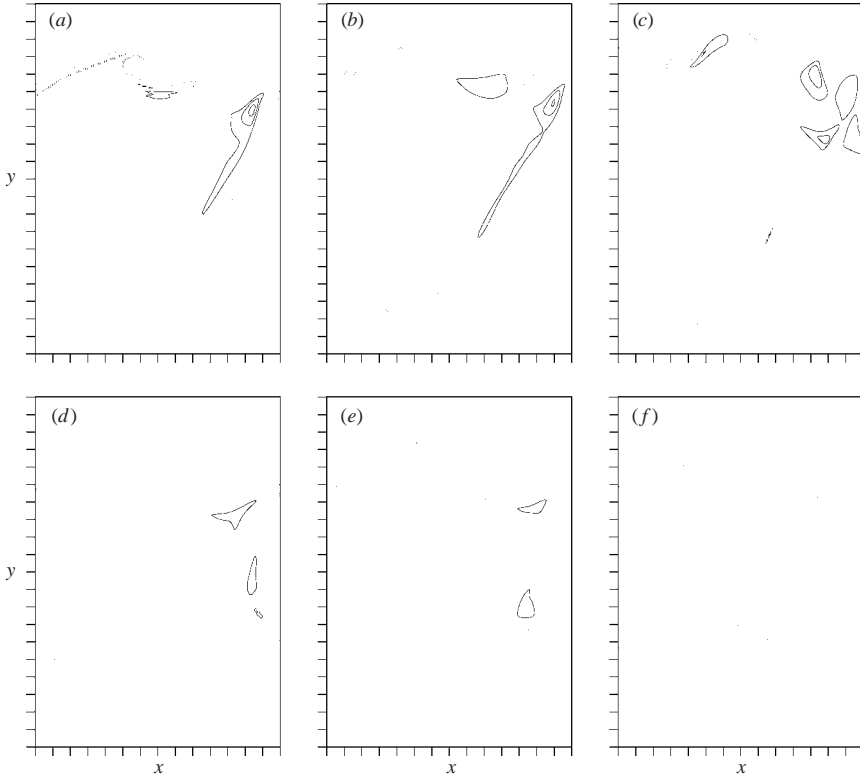


FIGURE 13. Contours of ω_z in the between-rib plane, showing the secondary roll-up of the spanwise vortical sheets in (a), (b), (c) a Newtonian mixing layer at $Re=200$ and (d), (e), (f) a viscoelastic mixing layer at $Re=200$, $We=20$, $b=400$ and $k=0.9$. Solid contours indicate positive vorticity and dotted contours indicate negative vorticity. (a) $t=90$ ($-1.9, 0.5$). (b) $t=100$ ($-1.6, 0.5$). (c) $t=110$ ($-2.2, 0.25$). (d) $t=90$ ($-1.4, 0.1$). (e) $t=100$ ($-0.8, 0.1$). (f) $t=110$ ($-0.9, -0.1$).

the intensities of the ribs and the thin sheets not only results from the weakened quadrupoles, but from the direct effect of viscoelasticity and the weakened cups, although the latter two effects are expected to be less pronounced. In addition, the inhibition of the development of the spanwise vortices with sign opposite to that of the cups is also considerable after $t=60$ in the viscoelastic mixing layer (figure 8b), and the mechanism is simple if we consider that their vorticity enhancement is due to the inductions by the cups, the quadrupoles and the ribs.

We have seen that viscoelasticity weakens the intensities of all large-scale vortical structures in the mixing layer. The experiments (Hibberd *et al.* 1982; Riediger 1989) showed that the large-scale structures existed longer in the viscoelastic mixing layer than in the Newtonian one. A reasonable explanation is that weaker large-scale structures may have longer lifetimes because stronger vortices, generally speaking, break down into smaller-scale vortices more quickly. For example, the quadrupoles in the viscoelastic fluids are found to be able to survive a longer time (figure 14). Diminution of small-scale structures observed in the experimental viscoelastic mixing layer (Hibberd *et al.* 1982; Riediger 1989) can be explained by consideration of two factors, based on our numerical results: one is that breakdown of weaker large-scale vortices results in fewer smaller-scale vortices, as illustrated in figure 14, and the

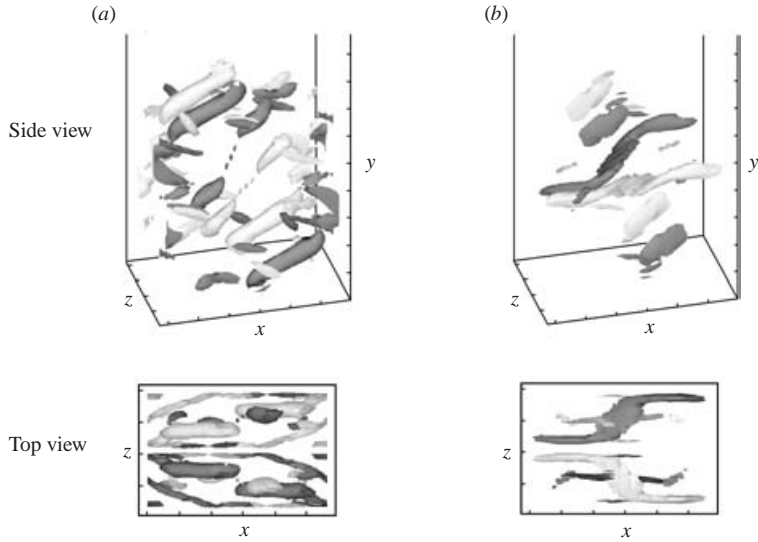


FIGURE 14. Iso-surfaces of the streamwise vorticity ω_x in (a) a Newtonian mixing layer ($Re=200$) and (b) a viscoelastic one ($Re=200$, $We=20$, $b=400$ and $k=0.9$) at $t=100$. Dark surfaces indicate positive vorticity of 0.5 and light surfaces indicate negative vorticity of -0.5 .

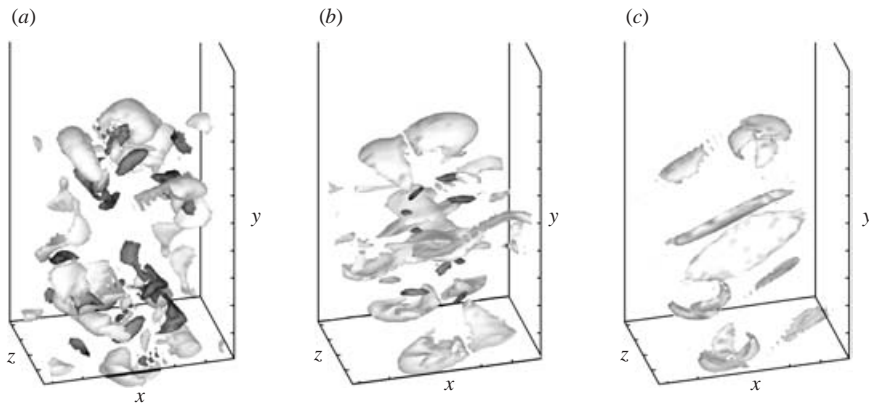


FIGURE 15. Iso-surfaces of the spanwise vorticity ω_z in (a) a Newtonian mixing layer ($Re=200$), (b) a viscoelastic one ($Re=200$, $We=20$, $b=400$ and $k=0.9$) and (c) a viscoelastic one ($b=900$) at $t=110$. Dark surfaces indicate positive vorticity of 0.3 and light surfaces indicate negative vorticity of -0.3 .

other is that there is a tendency for the small-scale structures in the core region to merge into large-scale ones in the viscoelastic case (figures 15 and 16). For $b=900$, a flat and inclined vortex forms at $t=110$ (figures 15c and 16c), which resembles the structure of the type observed in an experimental mixing layer with surfactants injected (Riediger 1989).

It was found that the velocity fluctuations were enhanced along the flow direction and suppressed along the other two in the wall-bounded shear turbulence due to polymer additives (e.g. Wei & Willmarth 1992; Dimitropoulos *et al.* 1998). In the viscoelastic mixing layer of a 50 p.p.m. polyacrylamide solution at Reynolds number of the order of 10^4 , Hibberd *et al.* (1982) observed that the streamwise and the

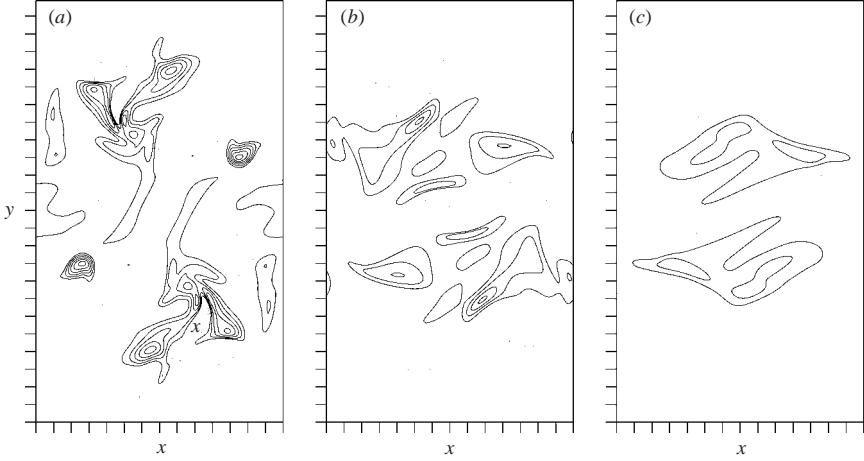


FIGURE 16. Contours of ω_z in (a) a Newtonian mixing layer ($Re = 200$), (b) a viscoelastic one ($Re = 200$, $We = 20$, $b = 400$ and $k = 0.9$) and (c) a viscoelastic one ($b = 900$) in the rib plane (RP) at $t = 110$. Solid contours indicate positive vorticity and dotted contours indicate negative vorticity. (a) $t = 110(-1.3, 0.6)$. (b) $t = 110(-0.7, 0.4)$. (c) $t = 110(-0.7, 0.2)$.

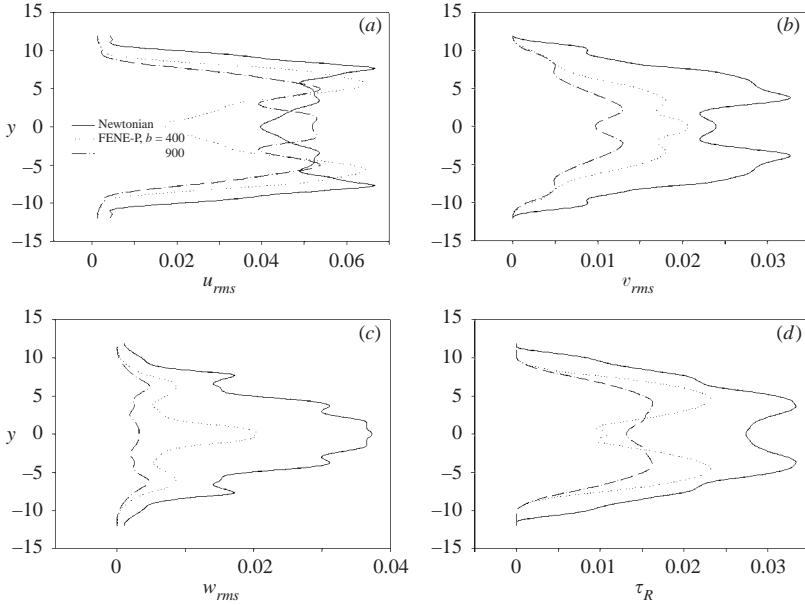


FIGURE 17. Root mean square (r.m.s.) velocity fluctuations: (a) U_{rms} , (b) V_{rms} , (c) W_{rms} and (d) Reynolds turbulence stress τ_R as functions of the transverse position. $Re = 200$, $We = 20$ and $k = 0.9$.

transverse velocity fluctuations and the Reynolds stresses were all lower upstream but higher downstream compared to those in the corresponding Newtonian mixing layer. On the other hand, Riediger (1989) reported that in the 900 p.p.m. surfactant solution, the streamwise velocity fluctuation in the vicinity of the centre of the mixing layer was stronger, and the transverse velocity fluctuation and the Reynolds stress were lower than in the Newtonian fluids irrespective of the streamwise positions. Figure 17 plots the calculated velocity fluctuations in all three directions and the

Reynolds stress at $t = 110$, from which we can see that all quantities are suppressed by polymer additives and the suppression of W_{rms} is more pronounced than the others, in particular U_{rms} , indicating that the diminution of the intensities of the streamwise vortical structures is the most essential effect of viscoelasticity, consistent with the analysis of vorticity dynamics presented earlier. Our Reynolds number is much lower than used in the experiments and the transition to turbulence of our viscoelastic mixing layers is obstructed, thus it is more suitable to compare our results with those of Hibberd *et al.* (1982) at upstream than downstream – a qualitative agreement is found here. It is interesting that the vortical structures for $b = 900$ at $t = 110$ in our simulations are similar to those observed in the surfactant solution, as mentioned earlier, and accordingly, the velocity fluctuations and the Reynolds stress for both solutions are also in qualitative agreement.

It has been observed that, in wall-bounded flows, the maximum polymer extension occurs on the edge of streamwise vortices that typically appear in counter-rotating pairs, and the turbulent fluctuation that cause transport of polymer from the vortex surface to the core can in turn influence the dynamics of these vortices. In our mixing layer, we have observed that the enormous polymer extension also appears on the edge of the streamwise vortices, but the transport of the polymer from the edge to the core is not a necessary condition for influencing the dynamics of the vortices, since the stretching of polymer on the edge of the vortices can diminish the vorticity there and even cause the opposite-signed vorticity, and consequently affect the vortex dynamics.

Dye visualization is the main method used in experiments to demonstrate the effects of viscoelasticity on the coherent structures. To produce a numerical dye visualization, we plot the contours of the passive scalar at $t = 90, 100$ and 110 in the rib plane and the between-rib plane in figures 18 and 19, respectively. The passive scalar, are controlled by the vortical structures; figures 18 and 19 confirm that the inhomogeneity of the flow is greatly inhibited by polymer additives.

3.2.3. Effects of b and We

The flow dynamics in the three-dimensional case is much more complex than in the two-dimensional case, hence, it is necessary to inspect to what extent the accuracy of our results is affected by the stress artificial diffusion, although we have verified that its effect on the two-dimensional flow dynamics is marginal. It is not possible to obtain the flow fields substantially modified by viscoelasticity without introducing the artificial diffusion in the three-dimensional case owing to the prohibitively high computational cost, and what we can do is to check the mesh convergence of the results in the presence of the artificial diffusion. In addition, the introduction of the free-slip boundary condition at a finite transverse position may question our numerical model as an appropriate approximation to a mixing layer when the vortices approach close to the boundary. Therefore, we plot in figure 20 the time developments of the maximum streamwise vorticity and U_{rms} at $t = 110$ obtained at the coarser mesh resolution of $64 \times 128 \times 64$ and the enhanced L_2 of 28, respectively, for the case of $Re = 200$, $We = 20$, $b = 400$ and $k = 0.9$. The differences between the results for $L_2 = 24$ and $L_2 = 28$ are not discernible except for U_{rms} near the boundary, indicating that L_2 of 24 is large enough to achieve an excellent approximation over the simulation time covered. The results for the mesh resolution $64 \times 128 \times 64$ do not differ significantly from those for $128 \times 256 \times 64$, in particular before $t = 90$, indicating that the results presented in this study are reasonably accurate and our adaptive method for introducing the artificial diffusivity is very effective.

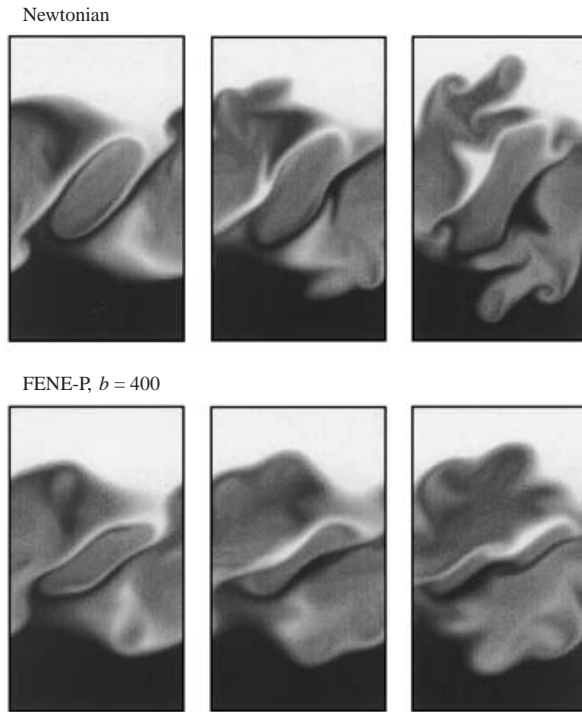


FIGURE 18. Contours (grey colourmap) of the passive scalar in the rib plane (RP) at $t = 90$, 100 and 110 for different fluids.

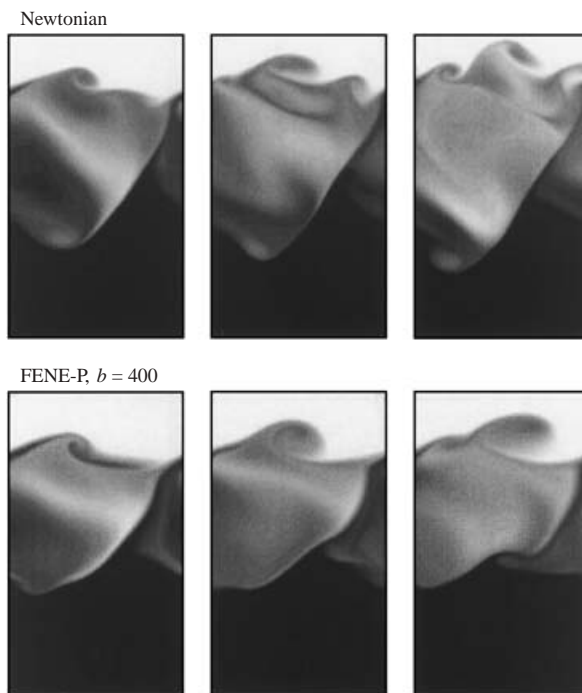


FIGURE 19. Contours (grey colourmap) of the passive scalar in the between-rib plane (BP) at $t = 90$, 100 and 110 for different fluids.

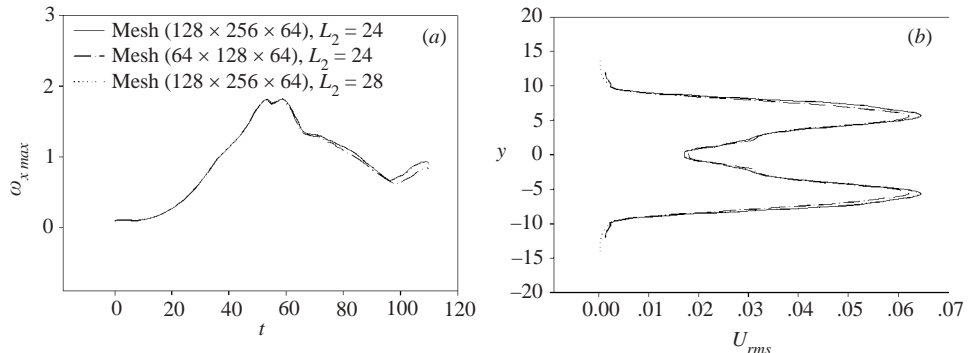


FIGURE 20. Convergence tests for the mesh and L_2 : (a) evolution of the maximum streamwise vorticity and (b) U_{rms} at $t = 110$. $Re = 200$, $We = 20$, $b = 400$ and $k = 0.9$.

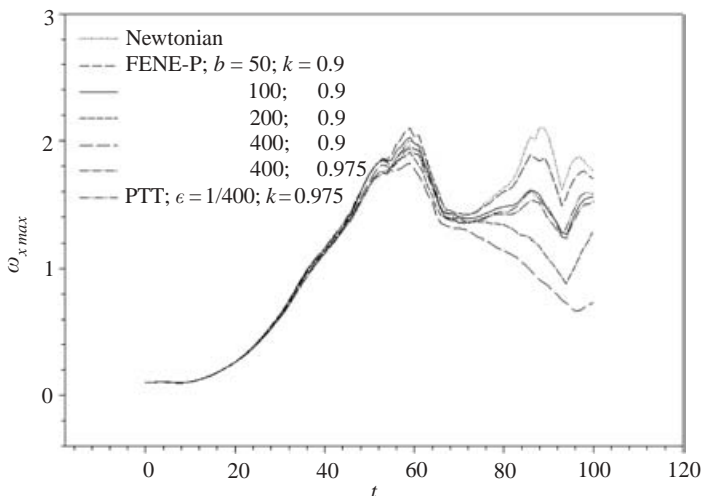


FIGURE 21. Effects of b for the FENE-P model on $(\omega_x)_{max}$. The curve for the PTT model is plotted for inspecting the role of the extensional viscosity. $Re = 200$ and $We = 20$.

Since the mesh resolution $64 \times 128 \times 64$ can give predictions with acceptable accuracy, we use it to compute the flows for examining the effects of b and We on the flow dynamics. The results are shown in figures 21 and 22, from which, we can see that the developments of the streamwise structures, not surprisingly, are inhibited more significantly at higher b and We . The results of Dimitropoulos *et al.* (1998) showed that the extensional viscosity was an important quantity to account for the polymer-induced drag reduction in the turbulent channel flow and the velocity fluctuations were almost exclusively determined by the extensional viscosity at a fixed We . For a steady uniaxial extensional flow of the FENE-P fluids, the extensional viscosity is given by

$$\frac{\eta_e}{\eta_0} = 3[k + (1 - k)\xi], \quad (3.1)$$

in which ξ is a function of b and $We\dot{\epsilon}$, $\dot{\epsilon}$ being the dimensionless extensional strain rate. The value of ξ is almost unity at small $We\dot{\epsilon}$ and approaches $2b/3$ at large

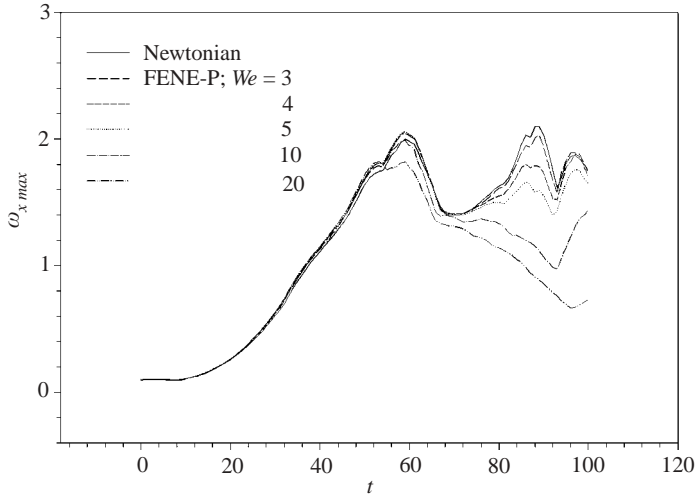


FIGURE 22. Effects of We for the FENE-P model on $(\omega_x)_{\max}$. $Re=200$, $b=400$ and $k=0.9$.

$We\dot{\epsilon}$. For the unsteady complex flows such as the mixing layer studied here, it is not possible to determine an equivalent extensional strain rate that is independent of the other parameters. Therefore, we only match the extensional viscosity by adjusting the values of k and b , as Dimitropoulos *et al.* (1998) did. From equation (3.1), the system with $k=0.9$ and $b=100$ matches the one with $k=0.975$ and $b=400$ in terms of the extensional viscosity at infinitely large $We\dot{\epsilon}$. Actually, infinitely large $We\dot{\epsilon}$ is not a necessary condition for this match, and the match is valid as long as ξ is a linear function of b , which seems to approximately hold at $We\dot{\epsilon} = O(1)$, and $b \gg 1$, according to equation (3.1). Figure 21 confirms that the extensional viscosity is also an important quantity to determine the extent to which the coherent structures in a mixing layer are modified by polymer additives.

The affine PTT model (Phan-Thien & Tanner 1977) takes the form

$$[1 + \epsilon \text{tr}(\mathbf{B} - \mathbf{I})](\mathbf{B} - \mathbf{I}) + We \left(\frac{\partial \mathbf{B}}{\partial t} + \mathbf{v} \cdot \nabla \mathbf{B} - \nabla \mathbf{v}^T \cdot \mathbf{B} - \mathbf{B} \cdot \nabla \mathbf{v} \right) = 0, \quad (3.2)$$

$$\boldsymbol{\tau} = \frac{(1-k)}{We} (\mathbf{B} - \mathbf{I}), \quad (3.3)$$

in which ϵ represents the extensibility of the polymer and is equivalent to $1/b$ in the FENE-P model, since the limiting value of ξ is $2/3\epsilon$. Figure 21 shows that the affine PTT model and the FENE-P model produce essentially the same results at the same extensional viscosity, which further corroborates the importance of the extensional viscosity, and on the other hand, indicates that the affine PTT model is also a good model to describe the flow of the drag-reducing polymer. The effects of the polymer normal stresses on the flow dynamics are marginal at either small We or small b irrespective of how large the other one is, as indicated in figures 21 and 22.

4. Conclusions

For the forced three-dimensional mixing layer and the parameter ranges studied, the effect of polymer additives on formation of the coherent structures, including the

quadrupoles, the ribs, the cups and the spanwise vortices rotating in the opposite direction to that of the cups, is found to be negligible ($t < 50$). The polymer normal stresses develop wherever there exist extensional strains that are produced by the coherent structures. They then hinder the development of these structures. Stretching by the quadrupoles and the ribs together at the between-rib plane region gives rise to enormous enhancement of the polymer normal stress differences there. These normal stress differences diminish the intensities of the quadrupoles, the cups and the ribs, which further inhibit growth in the spanwise vorticity with opposite sign to that of the mean vorticity. In the viscoelastic case, weaker intensity of the quadrupoles leads to weaker ribs, weaker spanwise vortical sheets and weaker secondary roll-up of the sheets. Attenuation of these large-scale structures results in a diminution of small-scale structures after their breakdown. There is a tendency of the small-scale structures in the core region to merge into a large-scale one in the viscoelastic case, as a result, a flat and inclined vortex forms which resembles the type of structure observed in an experimental mixing layer with surfactants injected. The extensional viscosity is an important quantity to determine the extent to which the coherent structures in a mixing layer are modified by polymer additives.

We wish to thank Professor Roger I. Tanner for helpful discussions and the referees for their invaluable comments and suggestions. Z. Y. gratefully acknowledges an IPRS scholarship from the Australian government and an IPA scholarship from the University of Sydney. The computations were performed on the workstations at the Bioengineering Division at the National University of Singapore.

Appendix. Solution of the FENE-P model in a steady shear flow

Consider the following dimensional FENE-P constitutive equations:

$$f\mathbf{B} + \lambda \left(\frac{\partial \mathbf{B}}{\partial t} + \mathbf{v} \cdot \nabla \mathbf{B} - \nabla \mathbf{v}^T \cdot \mathbf{B} - \mathbf{B} \cdot \nabla \mathbf{v} \right) = \mathbf{I}, \quad (\text{A } 1)$$

$$\boldsymbol{\tau} = \frac{\eta_p}{\lambda} (f\mathbf{B} - \mathbf{I}), \quad (\text{A } 2)$$

$$f = \frac{1 - 3/b}{1 - \text{tr}(\mathbf{B})/b}, \quad (\text{A } 3)$$

$$\mathbf{S} = 2\eta_s \mathbf{D} + \boldsymbol{\tau}, \quad (\text{A } 4)$$

where η_p is the polymer viscosity, \mathbf{S} is the total stress tensor, \mathbf{D} is the strain-rate tensor, and the other quantities have been defined in §2.

For a steady shear flow with the velocity profile $u = u(y)$, equation (A 1) yields

$$\left. \begin{aligned} \left(\frac{1 - 3/b}{1 - (B_{xx} + 2B_{yy})/b} \right) B_{xx} - 2W_s B_{xy} &= 1, \\ \left(\frac{1 - 3/b}{1 - (B_{xx} + 2B_{yy})/b} \right) B_{yy} &= 1, \\ \left(\frac{1 - 3/b}{1 - (B_{xx} + 2B_{yy})/b} \right) B_{xy} - W_s B_{yy} &= 0, \end{aligned} \right\} \quad (\text{A } 5)$$

where $W_s = \lambda du/dy$. The solution of the above set of equations is

$$\left. \begin{aligned} B_{xx} &= -\xi b + \xi + b, \\ B_{yy} &= B_{zz} = \xi, \\ B_{xy} &= W_s^2 \xi, \\ \xi &= \frac{1}{6W_s} \chi - \frac{b}{W_s} \frac{1}{\chi}, \\ \chi &= \sqrt[3]{6b(9W_s + \sqrt{3(2b + 27W_s^2)})}. \end{aligned} \right\} \quad (\text{A } 6)$$

Particularly, for a simple shear flow with the shear rate of $\dot{\gamma}$, from equations (A 2)–(A 4) and (A 6) we can obtain

$$\frac{\eta - \eta_s}{\eta_0 - \eta_s} = \xi, \quad (\text{A } 7)$$

where η is the viscosity defined by $\eta = S_{xy} / \dot{\gamma}$.

The solution for a steady uniaxial elongational flow can also be easily obtained, and is not given here for brevity.

REFERENCES

- ATSAVAPRANEE, P. & GHARIB, M. 1997 Structures in stratified plane mixing layers and the effects of cross-shear. *J. Fluid Mech.* **342**, 53–86.
- AZAIÉZ, J. 2000 Reduction of free shear flows instability: effects of polymer versus fibre additives. *J. Non-Newtonian Fluid Mech.* **91**, 233–254.
- AZAIÉZ, J. & HOMSY, G. M. 1994a Linear stability of free shear flow of viscoelastic liquids. *J. Fluid Mech.* **268**, 37–69.
- AZAIÉZ, J. & HOMSY, G. M. 1994b Numerical simulation of non-Newtonian free shear flows at high Reynolds numbers. *J. Non-Newtonian Fluid Mech.* **52**, 333–374.
- CADOT, O. & KUMAR, S. 2000 Experimental characterization of viscoelastic effects on two- and three-dimensional shear instabilities. *J. Fluid Mech.* **416**, 151–172.
- CANUTO, C., HUSSAINI, M. Y., QUARTERONI, A. & ZANG, T. A. 1987 *Spectral Methods in Fluid Dynamics*. Springer.
- DIMITROPOULOS, C. D., SURESHKUMAR, R. & BERIS, A. N. 1998 Direct numerical simulation of viscoelastic turbulent channel flow exhibiting drag reduction: effect of the variation of rheological parameters. *J. Non-Newtonian Fluid Mech.* **79**, 433–469.
- HIBBERD, M. F., KWADÉ, M. & SCHARE, R. 1982 Influence of drag reducing additives on the structure of turbulence in a mixing layer. *Rheol. Acta* **21**, 582–586.
- KUMAR, S. & HOMSY, G. M. 1999 Direct numerical simulation of hydrodynamic instabilities in two- and three-dimensional viscoelastic free shear layers. *J. Non-Newtonian Fluid Mech.* **83**, 249–276.
- LASHERAS, J. C. & CHOI, H. 1988 Three-dimensional instability of a plane free shear layer: an experimental study of the formation and evolution of streamwise vortices. *J. Fluid Mech.* **189**, 53–86.
- LEBOEUF, R. L. & MEHTA, R. D. 1996 Vortical structure morphology in the region of a forced mixing layer: roll-up and pairing. *J. Fluid Mech.* **315**, 175–221.
- LUMLEY, J. L. 1969 Drag reduction by additives. *Annu. Rev. Fluid Mech.* **1**, 367–384.
- MICHALKE, A. 1964 On the inviscid instability of the hyperbolic-tangent velocity profile. *J. Fluid Mech.* **19**, 543–556.
- MOSER, R. D. & ROGERS, M. M. 1991 Mixing transition and the cascade to small scales in a plane mixing layer. *Phys. Fluids A* **3**, 1128–1134.
- NYGAARD, K. J. & GLEZER, A. 1991 Evolution of streamwise vortices and generation of small scale motion in a plane mixing layer. *J. Fluid Mech.* **231**, 257–301.

- OLDAKER, D. K. & TIEDERMAN, W. G. 1977 Spatial structure of the viscous sublayer in drag-reducing channel flows. *Phys. Fluids* **20**, S133–S144.
- PHAN-THIEN N. & TANNER, R. I. 1977 A new constitutive equation derived from network theory. *J. Non-Newtonian Fluid Mech.* **2**, 353–365.
- PRESS, W. H., TEUKOLSKY, S. A., VETTERLING, W. T. & FLANNERY, B. P. 1996 *FORTRAN Numerical Recipes* (2nd edn). Cambridge University Press.
- RIEDIGER, S. 1989 Influence of drag reducing additives on a plane mixing layer. In *Drag Reduction in Fluid Flows* (ed. R. H. J. Sellin & R. J. Moses), pp. 303–310. Ellis Horwood.
- ROGERS, M. M. & MOSER, R. D. 1992 The three-dimensional evolution of a plane mixing layer: the Kelvin-Helmholtz rollup. *J. Fluid Mech.* **243**, 183–226.
- SURESHKUMAR R. & BERIS, A. N. 1995 Effect of artificial stress diffusivity on the stability of numerical calculations and the flow dynamics of time-dependent viscoelastic flows. *J. Non-Newtonian Fluid Mech.* **60**, 53–80.
- SURESHKUMAR R., BERIS, A. N. & HANDLER, R. A. 1997 Direct numerical simulation of turbulent channel flow of a polymer solution. *Phys. Fluids* **9**, 743–755.
- WEI, T. & WILLMARTH, W. W. 1992 Modifying turbulent structure with drag-reducing polymer additives in turbulent channel flows. *J. Fluid Mech.* **245**, 619–641.
- YARIN, A. L. 1997 On the mechanism of turbulent drag reduction in dilute polymer solutions: dynamics of vortex filaments. *J. Non-Newtonian Fluid Mech.* **69**, 137–153.
- YU, Z., LIN, J. & FAN, X. 1999 Numerical simulation of interactions between rigid rod-like polymers and coherent structures in a mixing layer. *J. Non-Newtonian Fluid Mech.* **83**, 1–18.